

Thermo-Mechanical Finite Element Modeling of the Friction Drilling Process

Scott F. Miller

Albert J. Shih

Department of Mechanical Engineering,
University of Michigan,
Ann Arbor, MI 48109

Friction drilling uses a rotating conical tool to penetrate the workpiece and create a bushing in a single step without generating chips. This research investigates the three-dimensional (3D) finite element modeling (FEM) of large plastic strain and high-temperature work-material deformation in friction drilling. The explicit FEM code with temperature-dependent mechanical and thermal properties, as well as the adaptive meshing, element deletion, and mass scaling three FEM techniques necessary to enable the convergence of solution, is applied. An inverse method to match the measured and modeling thrust force determines a coefficient of friction of 0.7 in this study. The model is validated by comparing the thrust force, torque, and temperature to experimental measurements with reasonable accuracy. The FEM results show that the peak temperature of the workpiece approaches the work-material solidus temperature. Distributions of plastic strain, temperature, stress, and deformation demonstrate the thermomechanical behavior of the workpiece and advantages of 3D FEM to study of work-material deformation in friction drilling. [DOI: 10.1115/1.2716719]

1 Introduction

Friction drilling utilizes the heat generated by friction between a rotating conical tool and work-material to soften and penetrate the thin-walled workpiece to make a hole [1–8]. The heat increases ductility of the work material, which is extruded on to both the front and back sides of the hole. The process forms a bushing from the thin workpiece and is a clean, chipless hole-making process. The bushing can increase the depth for threading and the clamp load capability. Extensive research in friction drilling has been conducted on the workpiece metallurgical analysis [5], tool and workpiece temperature [6], tool wear [7], and petal formation in bushing of brittle cast metals [8]. Figure 1 shows the cross-sectional pictures of the deformed workpiece and tool at four stages in friction drilling a hole on 1.6 mm thick Al 6061-T6. In stage 1, the conical tool comes into contact with the workpiece. In stage 2, the tool has nearly penetrated the workpiece. The thrust force is typically at its peak, and the back extrusion of work material can be seen at this stage. Stage 3 shows the ductile work material encompassing the tool tip. The extrusion of material sideward to form a bushing can be identified. This is the tool location with the maximum torque in drilling. As the tool penetrates the workpiece in stage 4, the bushing of the 5.3 mm dia hole is formed. Some work material is back extruded at the entry of the hole.

The work-material deformation is very large, and both the tool and workpiece temperatures are high in friction drilling [6]. Modeling is a necessary tool to understand the material flow, temperatures, stresses, and strains, which are difficult to measure experimentally during friction drilling. A semi-empirical analytical model based on the contact pressure and measured temperature has been developed to predict the thrust force and torque in friction drilling [6]. This model is simple but not able to provide detailed analysis of the work-material deformation. This can be overcome by using the thermomechanical FEM to analyze the

high temperature and large deformation of the work material in friction drilling. This research effort is still lacking and becomes the goal of this study.

The finite element method (FEM) has been applied to simulate the friction stir welding (FSW), a process similar to friction drilling. In FSW, a rotating tool is used to generate frictional heat and stir the work material around the tool to join two parts. The only significant difference is that friction drilling displaces work material to form a hole, whereas FSW mixes and welds work material. Spot friction welding (SFW) or friction stir spot welding (FSSW) is a FSW process to join two sheets of metal in one spot [9]. This process is very similar to the friction drilling. Both processes have the rotating tool feeding in the axial direction. There is a lack of research in modeling of the friction drilling process. However, extensive FEM research in FSW, SFW, and FSSW has been conducted and becomes the basis of this study.

Research in modeling of FSW has been reviewed by Chao et al. [10], Schmidt and Hattel [11], and Soundararajan et al. [12]. Modeling of SFW has been conducted by Awang et al. [13] and Kakarla et al. [14] used the ABAQUS/EXPLICIT FEM program. The modeling of SFW is expanded in this research to investigate the friction drilling process.

In this study, the ABAQUS/EXPLICIT FEM software was utilized to simulate the thermomechanical behavior in friction drilling. The three-dimensional (3D), instead of two-dimensional (2D), FEM was chosen because the work material deforms in the rotational direction. Modeling results will show significant material flow in the rotational direction, particularly close to the contact area with the tool. The explicit method was well suited to solve the large work-material deformation and complex contact condition in friction drilling [15]. Three FEM techniques—adaptive meshing, element deletion, and mass scaling—are required to enable convergence of the FEM solution. Adaptive meshing and element deletion are necessary to maintain the mesh quality. Mass scaling is applied to increase the computational efficiency of the explicit method. The frictional heat generation and heat partition were implemented. A coupled thermomechanical analysis was performed with temperature-dependent thermal and mechanical properties of the work material.

Coulomb's friction law, which has been used extensively in FSW and SFW research [10–12,16–18], is adopted in this study. A wide range of Coulomb coefficients of friction has been reported

Contributed by the Manufacturing Engineering Division of ASME for publication in the JOURNAL OF MANUFACTURING SCIENCE AND ENGINEERING. Manuscript received July 10, 2006; final manuscript received January 3, 2007. Review conducted by Steven R. Schmid.

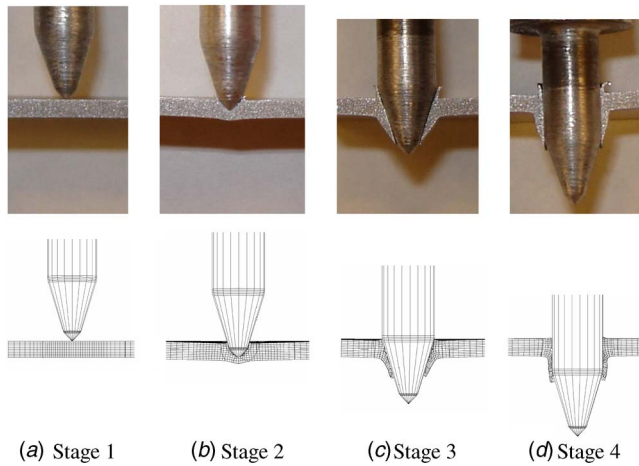


Fig. 1 Cross section of workpiece in experiment and modeling at four stages of tool location in friction drilling of 1.6 mm thick Al 6061 at tool travel of (a) 0 mm, (b) 2.77 mm, (c) 7.19 mm, and (d) 14.0 mm from the initial contact (5.3 mm hole diameter for scale)

in FSW and SFW. A coefficient of friction as high as 2.0 has been used in analytical modeling of FSW [16], taken from previously experimentally measured values. Soundararajan et al. [12] assumed the coefficient of friction ranging from 0.4 to 0.5 based on surface temperature and contact between tool and workpiece. Schmidt and Hattel [11] and Buffa et al. [17] had a constant coefficient of friction of 0.3 and 0.46, respectively. In SFW, Awang et al. [13] utilized the temperature-dependent coefficient of friction ranging from 0 to 0.62. Awang's model extrapolated between the published value of 0.62 from Serway [18] and 0 at the work-material melting temperature. Chao et al. [10] developed an inverse method for friction to match experimental and modeling results for temperature. This method is adopted in this study.

The dependence of coefficient of friction on different factors has not been determined; thus, the inputs to a better friction law are not available. The value of coefficient of friction depends on many factors, including sliding speed, contact pressure, temperature, material composition, etc. The coefficient of friction is very difficult to accurately quantify under complex contact conditions. Surface sliding conditions, including the contact pressure and speed, vary in friction drilling as the conical tool moves through the workpiece. Frictional heating at the tool-workpiece interface causes temperature in the workpiece to increase as sliding speed increases. This complicates experimental measurement of coefficient of friction because thermal and mechanical properties change with temperature. Research on a more comprehensive friction model is lacking and, therefore, the topic of future work.

In Sec. 2, the FEM of friction drilling is described. The experimental setup and validation by comparison of modeling and measured thrust force, torque, and temperature are then presented. Finally, FEM analysis of the deformed mesh, temperature, stress, nodal velocity, and contact force are discussed.

2 Friction Drilling FEM

Mathematical formulations of thermomechanical modeling are presented in this section.

2.1 Thermomechanical FEM Formulation. The friction and plastic deformation generate heat and elevate the workpiece temperature. The high temperature softens the workpiece and allows the work material to flow and form the hole and bushing. The governing equation for the thermal model of the work material is

$$\rho c \frac{\partial T}{\partial t} = k \left(\frac{\partial^2 T}{\partial x^2} + \frac{\partial^2 T}{\partial y^2} + \frac{\partial^2 T}{\partial z^2} \right) + G \quad (1)$$

where ρ is density, c is specific heat, k is heat conductivity, T is temperature, t is time, G is heat generation rate, and x , y , and z are spatial coordinates. ρ , c , and k are functions of temperature, which is important for accurate modeling of the friction drilling process. Both T and G are functions of x , y , z , and t . The heat generation rate G consists of the heating rate by the friction between tool and workpiece, \dot{q}_f , and heating rate from irreversible plastic deformation inside the workpiece, \dot{q}_p [13]

$$G = \dot{q}_f + \dot{q}_p \quad (2)$$

This study assumes that friction between the tool and workpiece follows Coulomb's friction law. The frictional force F_f is directly proportional to normal force F_n by the coefficient of friction μ , i.e., $F_f = \mu F_n$. The frictional heat generation rate \dot{q}_f is equal to F_f times the surface velocity of the tool V . At the local contact point with tool radius R , $V = 2\pi RN$, where N is the tool rotational speed. The frictional heat generation rate \dot{q}_f is

$$\dot{q}_f = 2\pi RN\mu F_n \quad (3)$$

The heat generation rate due to plastic deformation \dot{q}_p is

$$\dot{q}_p = \eta \sigma \dot{\epsilon}^{pl} \quad (4)$$

where η is the inelastic heat fraction, σ is the effective stress, and $\dot{\epsilon}^{pl}$ is the plastic straining rate. The energy from plastic deformation in the workpiece is small compared to that from friction to friction drilling. In this study, η is set to 0.9 [13].

The ABAQUS/EXPLICIT code used in this research integrates the equations of motion explicitly with respect to time. The term *explicit* means the state at the end of an increment is based solely on the displacements, velocities, and accelerations at the beginning of the increment [19]. The explicit expression for velocity at the new time step can be determined by applying the central difference integration.

2.2 FEM Techniques. Three FEM techniques—adaptive meshing, element deletion, and mass scaling—are deployed to enable convergence of the FEM solution in friction drilling modeling. The adaptive meshing and element deletion techniques are needed because the large deformation and excessively distorted elements are inevitable in friction drilling modeling. Adaptive meshing maintains a high-quality mesh throughout the solution by adjusting the mesh to restore aspect ratio of highly distorted elements [13]. Adaptive meshing does not alter the topology of the mesh. Elements are not created or destroyed from this feature. The improved mesh quality can prevent the divergence due to severe mesh distortion. In this study, the adaptive meshing was performed for every five increments of the tool.

The element deletion allows elements to separate and the tool to penetrate the workpiece [20] in friction drilling. Elements with excessively large plastic strain are deactivated. In this study, the criterion to delete an element is based on the value of the equivalent plastic strain. When the equivalent plastic strain exceeds a threshold value of 2.2 in an element, all the stress components are set to zero. This is the maximum value possible while maintaining convergence in the friction-drilling simulation. An example of element deletion during friction drilling is shown in Fig. 2. The dark color represents deleted elements, which do not affect the simulation results and can be removed from display of the results.

Mass scaling is employed to improve the FEM computational efficiency while retaining the accuracy. This technique adjusts the density of the work material to improve the time scale of analysis. The presence of small elements and reduced characteristic lengths of elements from deformation results in a smaller time increment of tool travel required for the simulation. Scaling the material density of the small elements throughout the simulation can significantly improve the stability in iteration and decrease the com-

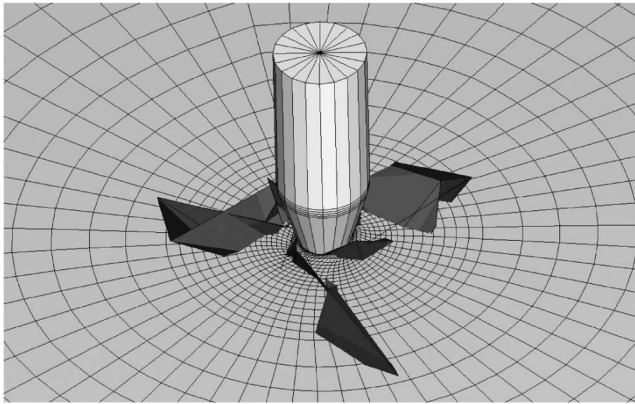


Fig. 2 Depiction of deleted elements (dark) in finite element modeling of friction drilling

putation time [19]. In this study, mass scaling is performed every ten increments to obtain a stable time increment of at least 0.0001 s step time of tool travel.

2.3 Mesh, Boundary Conditions, and Material Properties.

Figure 3 shows the initial FEM mesh, boundary conditions, and tool geometrical parameters in friction drilling. As shown in Fig. 3(a), the workpiece was 101.6 mm dia and 1.59 mm thick. Two opposite points on the workpiece were fixed to simulate the clamping by two C-clamps in the experiment. The top surface of the workpiece was under free convection with convection coefficient of 30 W/m² K and ambient air temperature of 22°C. The tool rotated at 3000 rpm or 314 rad/s. The tool penetration into the workpiece was modeled with three different constant axial speeds of 2.54 mm/s, 4.23 mm/s, and 5.93 mm/s.

The ABAQUS mesh generator was applied. Eight-node hexagonal elements were used to model the sheet-metal workpiece in the

shape of a disk plate. The initial finite element mesh in Figs. 3(a) and 3(b) includes 18,620 elements and 20,814 nodes. Each node had four degrees of freedom: three displacements in the X, Y, and Z directions and one nodal temperature. The workpiece mesh was finer near the tool tip, as shown in Fig. 3(b), where the largest material deformation was expected to occur. Across the 1.59 mm thickness of the workpiece, ten rows of elements were generated in the mesh. The element size was important for the simulation. If the mesh was too coarse, too many elements experienced severe distortion and were deleted, resulting in improper bushing formation. On the contrary, if the mesh was too fine, the computational time increased significantly without improving the results. A balance was struck between computational time and amount of workpiece mesh removed by element deletion.

Figure 3(c) shows the bottom view of the stationary, rigid support plate, which limits the movement of the workpiece in the Y direction. The node in contact with the support plate can move in the X and Z directions with the same coefficient of friction as in the tool-workpiece interface. The effect of friction between the workpiece and support plate is not significant because of the clamping restraint and their small relative motion. The support plate was 80 mm o.d. with a 24.5 mm dia hole. The friction drilling started at the center of the hole. The thermal boundary condition for the bottom of the workpiece was the combination of free convection (30 W/m² K convection coefficient) for the area exposed to air and adiabatic for the area in contact with the support plate.

The tool geometric parameters (Fig. 3(d)) of the tool used in this study are $\alpha=90$ deg, $\beta=36$ deg, $h_c=0.940$ mm, and $h_n=5.518$ mm. The tool is modeled as rigid and is not meshed. The vertical lines on the tool in Fig. 3 were generated by the ABAQUS program. Similar tool geometry has been used in previous research [5,7,8].

The work material is Al 6061-T6, a material commonly used in previous research of FSW FEM analysis. The temperature-dependent material properties for Al 6061-T6 are readily avail-

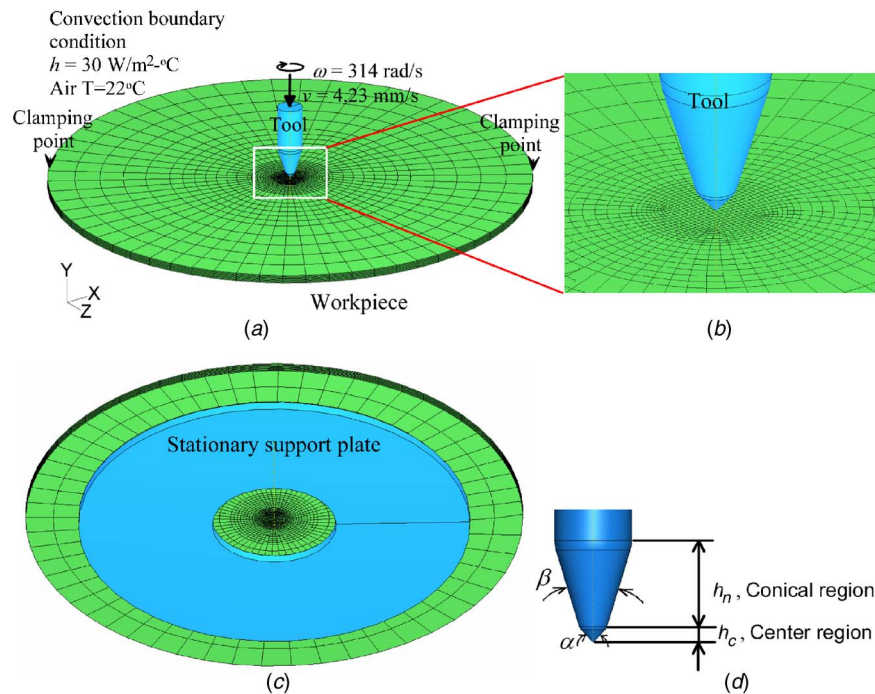


Fig. 3 Mesh, boundary condition, and tool geometry in friction drilling: (a) initial mesh and positions of the tool and workpiece, (b) close-up view of the mesh near the tool tip, (c) bottom view showing the stationary support plate, and (d) tool geometry and parameters

Table 1 Temperature-dependent material properties for aluminum 6061-T6 [12]

Temperature (°C)	37.8	93.3	149	204	260	316	371	427
Thermal conductivity (W/m°C)	162	177	184	192	201	207	217	223
Heat capacity (J/Kg°C)	945	978	1000	1030	1052	1080	1100	1130
Density (Kg/m ³)	2690	2690	2670	2660	2660	2630	2630	2600
Young's modulus (GPa)	68.5	66.2	63.1	59.2	54.0	47.5	40.3	31.7
Yield strength (MPa)	274	265	248	219	160	66.2	34.5	17.9
Thermal expansion (1/°C) × 10 ⁻⁶	23.5	24.6	25.7	26.6	27.6	28.5	29.6	30.7

able. Material properties used in this study are listed in Table 1 [21]. In FSW modeling, the elastoplastic model [13] was used. This simplified model is adequate in this research to model the work-material deformation in friction drilling. Nicholas [22] found that 6061-T6 aluminum alloy exhibits a very small sensitivity to high strain effects. For strain rates varying from 10⁻⁴ to 10⁴ s⁻¹ only minor changes in the yield stress occurred. Altenhof and Ames [23] showed that inclusion of strain rate effects in finite element simulations does not improve accuracy substantially for a proprietary aluminum alloy.

Frictional behavior and contact interaction between the tool and workpiece in friction drilling are complicated [7]. In this study, a constant coefficient of friction using Coulomb's friction law is adopted. This simple friction model is not adequate for the complicated friction phenomenon in friction drilling. However, a more comprehensive friction model is not available for implementation. The coefficient of friction was determined by matching the FEM results with varying coefficients of friction to experimentally measured thrust force and torque.

Heat partition occurs at the interface between the tool and workpiece. For frictional heat generation at the tool-workpiece interface, 100% of the dissipated energy caused by friction is assumed to be converted to heat. A common heat partition model based on the ratio of thermal conductivity of the tool and work materials determines the heat partition at the tool-workpiece interface. The ratio of heat partition into the workpiece, r_{wp} , is

$$r_{wp} = \frac{k_{wp}}{k_{wp} + k_{tool}} \quad (5)$$

where k_{wp} and k_{tool} are the thermal conductivity of workpiece and tool, respectively. At room temperature, k_{wp} of the Al 6061-T6 workpiece is 167 W/m K and k_{tool} of the A2 tool steel is 26 W/m K. The ratio of heat generated in the tool-workpiece interface transfer to the workpiece is $r_{wp}=0.87$, i.e., most of the frictional heat generated was transferred to the Al workpiece.

3 Experimental Setup

Experiments were conducted to measure the thrust force, torque, and workpiece temperature during friction drilling. Measurements were compared to FEM results for validation. The friction drilling experiment was conducted in a Mori Seiki TV 30 vertical machining center. The spindle speed was 3000 rpm and three tool feed rates were 2.54 mm/s, 4.23 mm/s, and 5.93 mm/s, which matched to the FEM inputs. The tool material was A2 air-hardening steel. The tool did not have the lobular geometry as in some commercial tools [7]. Dimensions of the tool matched to those used in modeling, as shown in Fig. 3(d).

The thrust force and torque was measured using a Kistler model 9272 dynamometer. The temperature was measured using a type-E thermocouple (Omega 5TC-TT-E-36-72) with 0.13 mm dia. Two separate drilling experiments were conducted for the measurement of workpiece temperature at points 5.1 mm and 7.5 mm from the center of drilling. Each experiment had two thermocouples embedded in two shallow, 1 mm dia holes 180 deg opposite from each other. Figure 4 shows two thermocouples embedded at points 7.5 mm from the drill center after friction drilling of a 5.3 mm dia hole.

4 Identification of Coefficient of Friction and Experimental Validation

Using the inverse method developed by Chao et al. [10], the experimentally measured thrust force and torque are compared to FEM results to identify the coefficient of friction. Based on this predicted coefficient of friction, the experimentally measured thrust force, torque, and workpiece temperature are compared to modeling results for model validation.

4.1 Coefficient of Friction. Figure 5 shows the thrust force and torque from experimental measurements and FEM analysis with three coefficients of friction, 0.5, 0.7, and 1.0 (4.23 mm/s feed rate and 3000 rpm spindle speed for the tool). High coefficient of friction causes a decrease in thrust force but does not change the torque significantly. Peak thrust forces of 1000 N, 800 N, and 600 N are observed for coefficients of friction of 0.5, 0.7, and 1.0, respectively. Coefficient of friction of 0.7 gives the best match for modeling and measured thrust force and torque. This value is used for all further FEM simulations in this study.

Figure 5 shows torque values are identical until ~7 mm of tool travel from contact. High coefficient of friction increases the frictional force and, subsequently, the torque. However, high coefficient of friction produces high temperature and soft work material from frictional heating to lower the torque. These two phenomena balance each other, which results in the small change in torque.

4.2 Validation of Thrust Force and Torque. With the coefficient of friction of 0.7, Fig. 6 shows the comparison of the modeled and measured thrust force and torque at three different tool feed rates, 5.93 mm/s, 4.23 mm/s, and 2.54 mm/s. The agreement between experimental and modeling of thrust force and torque validates the coefficient of friction of 0.7. The peak forces in the experiment were about 800 N, 750 N, and 700 N for feed rates of 5.93 mm/s, 4.23 mm/s, and 2.54 mm/s, respectively. These values were slightly higher in the FEM analysis.

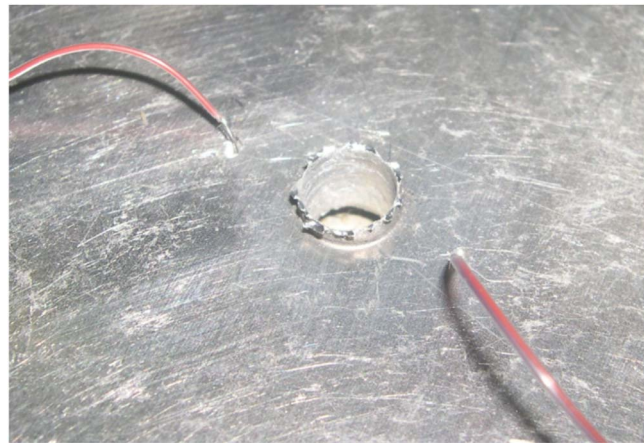


Fig. 4 Two thermocouples embedded in small holes 7.5 mm from the center of drilling for temperature measurement (5.3 mm dia drilled hole for scale)

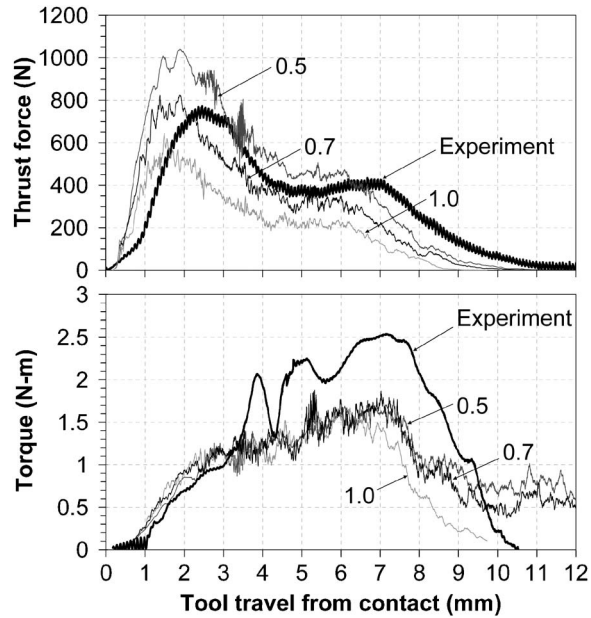


Fig. 5 Comparison of modeling thrust force and torque for different friction coefficients (4.23 mm/s feed rate and 3000 rpm spindle speed)

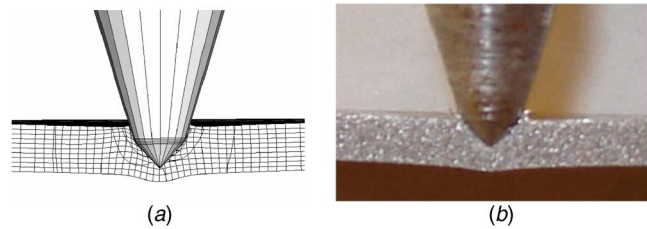


Fig. 7 Comparison of the tool-workpiece position at peak thrust force (a) FEM, 1.78 mm, and (b) experiment, 2.75 mm, tool travel from the initial tool-workpiece contact (4.23 mm/s tool feed rate)

The FEM thrust force profiles were shifted to the left of the experimental profiles, as shown in Fig. 6. This is due to the noticeable deflection of the sheet Al workpiece at the initial contact stage. This phenomenon was not accurately modeled by FEM and led to the early peak of the thrust force in FEM analysis. Figure 7 shows the relative position of tool to workpiece near peak thrust force for both FEM (Fig. 7(a)) and experiment (Fig. 7(b)) with 4.23 mm/s tool feed rate. The penetration of the tool into the workpiece is approximately the same, but the actual tool travel from the initial contact was 1.78 mm in FEM and 2.75 mm in

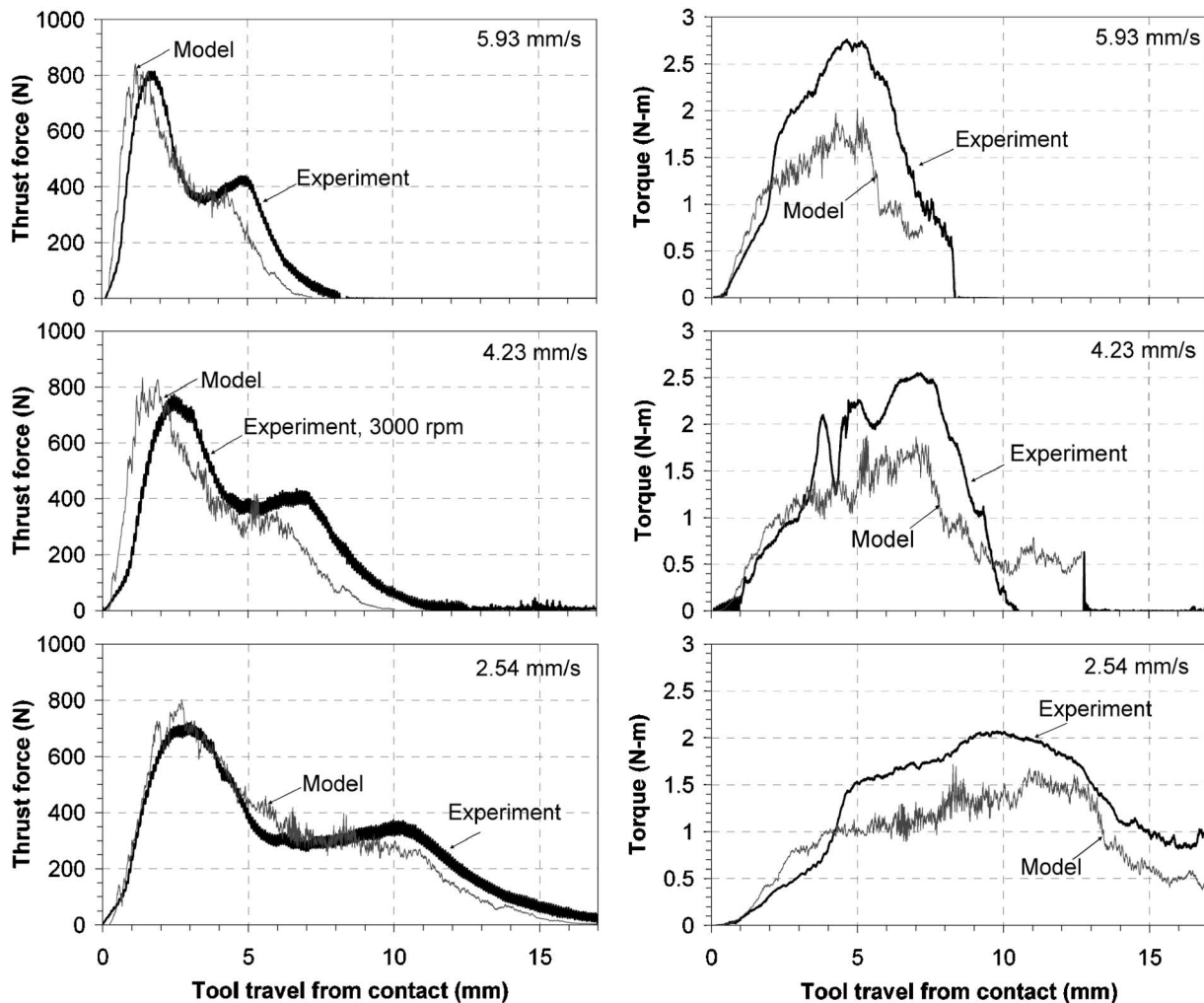


Fig. 6 Comparison of the experiment versus model predicted thrust force and torque in friction drilling for 0.7 coefficient of friction (3000 rpm spindle speed and 5.93 mm/s, 4.23 mm/s, and 2.54 mm/s feed rates).

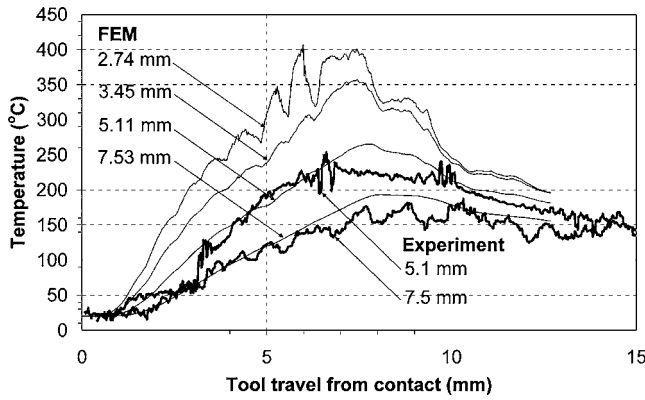


Fig. 8 FEM modeling and experimental measurement of temperature in friction drilling, numbers represent distance from hole center (0.7 coefficient of friction, 3000 rpm spindle speed, and 4.23 mm/s tool feed rate)

experiment. The 1 mm more tool travel in experiment (Fig. 7(b)) shows the larger workpiece deflection in experiment and the limitation of FEM at high tool feed rates.

At the lowest tool feed rate (2.54 mm/s), the effect of workpiece deflection is less significant; thus, the FEM prediction matches better with the experiment, as shown in Fig. 6. The slower tool feed rate allows more time for heat generation and work-material softening, which generates lower thrust force and smaller workpiece deflection.

For torque, as shown in Fig. 6, the discrepancy of modeling and experiment also improves at low tool feed rate. The model over-

estimated the torque in the initial contact stage, but underestimated the torque as it approaches its maximum. The maximum torque was underestimated by about 33%, 32%, and 25% for tool rate of 5.93 mm/s, 4.23 mm/s, and 2.54 mm/s, respectively. As discussed in Sec. 6.1 and shown in Fig. 5, adjusting the coefficient of friction has little effect on torque in the model. This demonstrates the limitation of the Coulomb's friction model and the need to implement new friction models to achieve a more accurate prediction of the torque in friction drilling modeling.

4.3 Validation of Workpiece Temperature. Figure 8 shows the comparison of measured workpiece temperature with FEM predictions at 4.23 mm/s tool feed rate. The model temperatures at four points, 2.74 mm, 3.45 mm, 5.11 mm, and 7.53 mm initial position from the hole center are presented. The measured temperatures from thermocouples embedded at points 5.1 mm and 7.5 mm from the hole center match well with FEM prediction and further validate the model developed in this study.

Other thermocouples installed closer to the hole center did not obtain a temperature reading. They were damaged during the experiment by the workpiece deformation. This demonstrates the difficulty to experimentally investigate friction drilling and the need for FEM analysis. The temperature is higher close to the hole center. Modeling results show the peak temperatures are 400°C, 350°C, 270°C, and 190°C at 2.74 mm, 3.45 mm, 5.11 mm, and 7.53 mm from the hole center, respectively.

5 FEM Analysis of Work-Material Deformation and Temperature

One advantage of FEM is insight into the work-material deformation and temperature, which are difficult to measure experimentally during friction drilling. Figure 9 shows the deformed

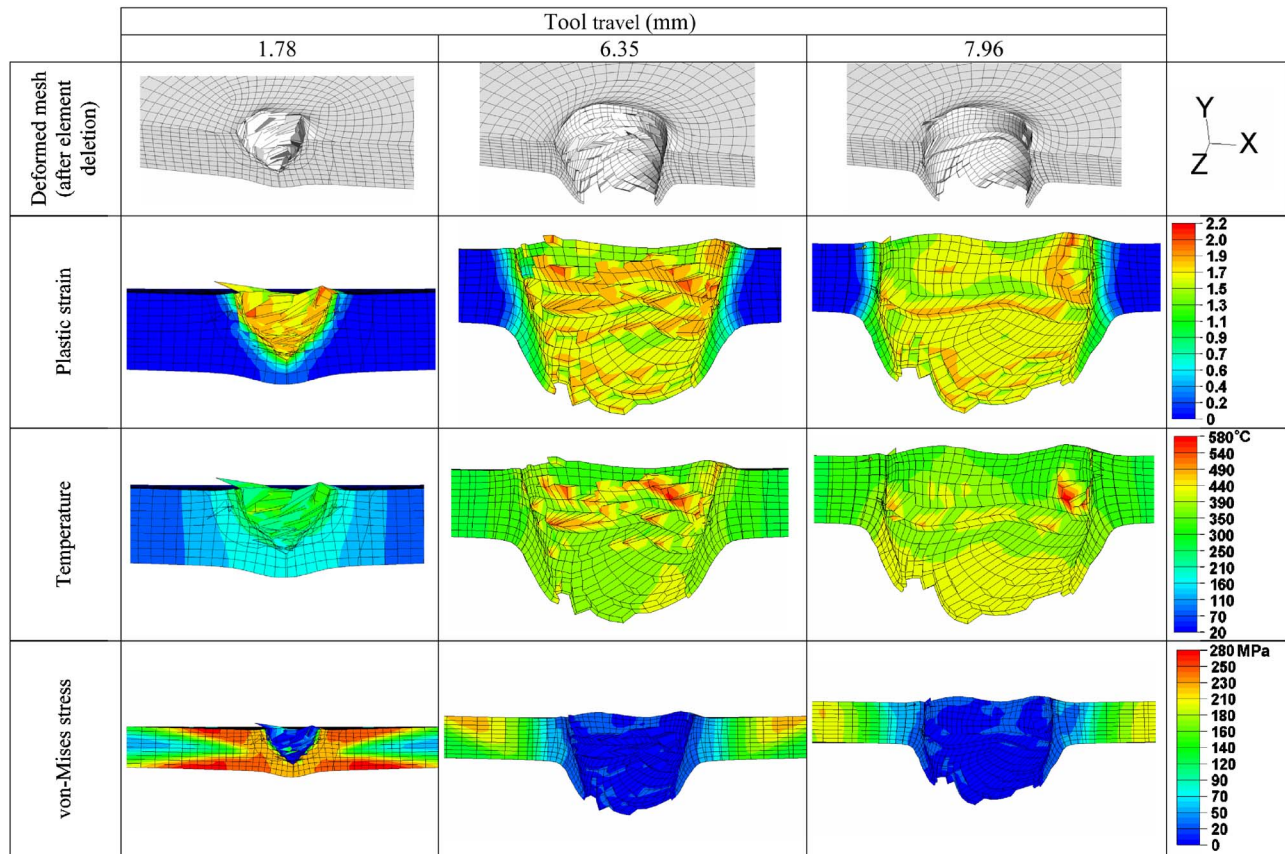


Fig. 9 Deformed mesh and distribution of plastic strain, temperature, and von Mises stress (4.23 mm/s feed rate, 3000 rpm spindle speed, 0.7 coefficient of friction)

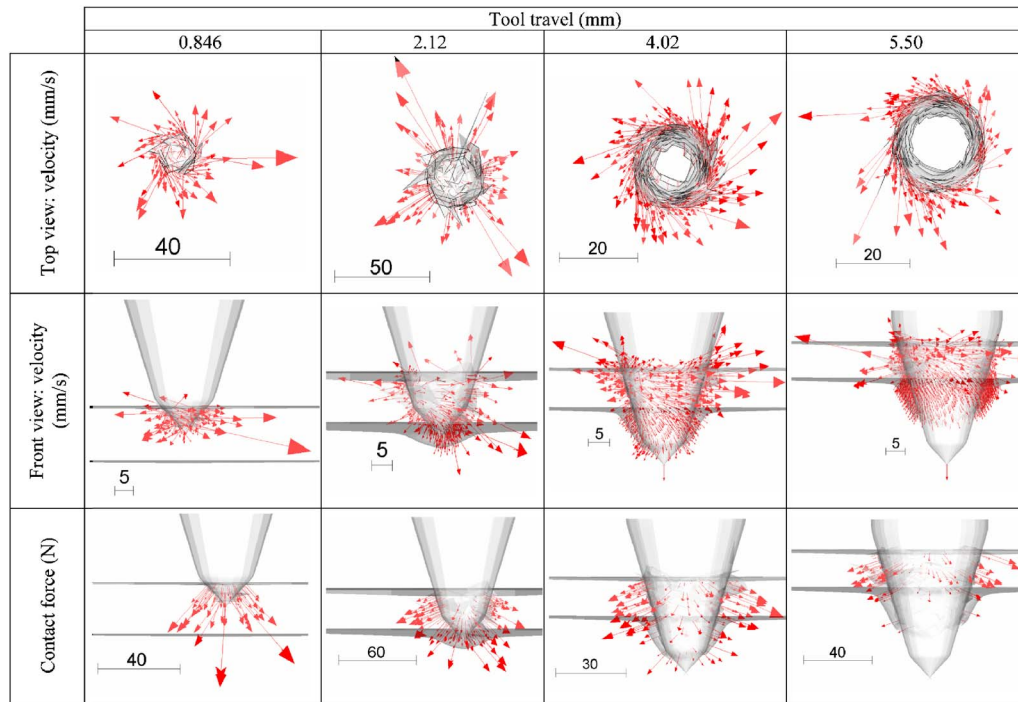


Fig. 10 Nodal velocity and force vectors at four tool locations

mesh and distribution of plastic strain, temperature, and von Mises stress of the cross section of the workpiece at 1.78 mm, 6.35 mm, and 7.96 mm tool travel from the contact between tool and workpiece. The tool travel of 1.78 mm and 6.35 mm are near the peak thrust force and peak torque, respectively. Figure 10 shows vectors for velocity and contact force at 0.846 mm, 2.12 mm, 4.02 mm, and 5.50 mm tool displacement. Process parameters for Figs. 9 and 10 were 4.23 mm/s tool feed rate and 3000 rpm spindle speed. All deleted elements were excluded in Figs. 9 and 10. The deformed mesh and plastic strain, temperature, von Mises stress, nodal velocity, and nodal contact force are discussed in Secs. 5.1–5.4.

5.1 Deformed Meshes and Plastic Strain. The cross-sectional view of the deformed mesh at four stages of friction drilling is shown in Fig. 1. The cross section of FEM predicted material deformation and bushing formation match well with experimental observations. The effect of element deletion on the prediction of bushing shape was a concern. As shown in Fig. 1(d), comparing the shape of bushing at the end of tool penetration at stage 4, element deletion does not significantly change the shape of bushing. However, the extrusion on the top of the workpiece is largely missing in stage 4. This is likely caused by the element deletion in the narrow region of work material under large strain.

A more detailed view of the deformed mesh is shown in Fig. 9. Shearing of the elements from right to left is evident on the inside wall of the hole. The distortion of elements is already very severe in the initial contact at 1.78 mm tool travel. The severely distorted elements are likely to contribute to the lack of modeling accuracy to predict the workpiece deflection and contact force in the beginning of contact at high tool feed rates.

The peak plastic strain is on the contact surface with the tool, as shown in Fig. 9. The peak plastic strain is about the same, 2.2, independent of the tool travel. This can be explained by the element deletion, which removes overly-distorted elements with the plastic strain over 2.2.

5.2 Temperature. Friction drilling temperature measurements have been conducted using the infrared camera [6] and by thermocouples in this study. FEM predicted temperature is more com-

prehensive. As shown in Fig. 9, at 1.78 mm of tool travel, temperature is not high, $\sim 300^\circ\text{C}$ on the contact surface. At 6.35 mm of tool travel, a stripe of high temperature close to 580°C is observed along the contact area within the originally undeformed workpiece. Work-material temperature is the highest on contact surface with the tool. The peak temperature region is concentrated on the hole surface where the tool contacts the original sheet metal workpiece. The experimental observation of discoloration on the AISI 1020 sheet metal workpiece in Ref. [6] supports this finding of the high-temperature region. The maximum temperature occurs at the tool location near the maximum torque, again supported by the experimental measurements in Ref. [6].

The peak temperature of workpiece is high in friction drilling. For Al 6061-T6, the solidus and liquidus temperatures are 582°C and 652°C , respectively. The maximum temperature predicted by FEM approaches the workpiece solidus temperature. The high-temperature zone in friction drilling is shallow. Away from the tool-workpiece contact surface, temperature decreases rapidly in bushing and workpiece.

5.3 von Mises Stress. von Mises stress is shown in the last row of Fig. 9. Contrary to intuition, the stress is low on the tool-workpiece contact surface due to the high temperature in the area. At 1.78 mm tool travel, the maximum stress of 280 MPa can be seen in the workpiece away from the hole. This high stress is due to the bending of the workpiece in the low-temperature region. At 6.35 mm and 7.96 mm tool travel, the peak stress of $\sim 230 \text{ N/mm}^2$ occurs further away from the hole in the workpiece.

Distributions of stress and temperature demonstrate the role of frictional heating in the work material. The high temperature softens the work material in the contact region and makes the bushing formation possible.

5.4 Nodal Velocity Vectors. Figure 10 shows the top and front views of velocity vectors at nodes on the contact surface. Only nodes with velocity larger than 2 mm/s are presented for clarity. Velocity vectors in the radial and tangential directions represent axisymmetrical and circumferential deformation, respec-

tively. The top view shows the deformation is mostly in the tangential direction. In this case, the axisymmetrical FEM is not adequate to model such deformation. The 3D FEM model is required to model the material flow in the combined rotational and radial directions. In the front view, near the top of the workpiece, vectors are pointing upward, indicating back extrusion. On the bushing, small downward velocity vectors represent the gradual formation of the bushing.

5.5 Nodal Contact Force Vectors. The last row in Fig. 10 shows vectors representing the contact force between the tool and workpiece. Most of the contact force vectors appear normal to the tool surface. The largest nodal contact force (46.4 N) occurs at 2.12 mm tool travel, near the peak thrust force in friction drilling. The contact force is also high in the tool tip region at 0.846 mm tool travel. At 4.02 mm and 5.50 mm tool travel, the contact forces on the bushing are small, as most of the contact force vectors are observed in the region of the undeformed sheet. In the analytical model to predict thrust force and torque in friction drilling [6], a hypothesis was proposed that the tool contact surface with bushing does not contribute to the thrust force and torque. This observation directly supports this hypothesis.

6 Conclusions

The 3D FEM model was demonstrated capable of modeling the work-material deformation and temperature in friction drilling by comparison to experimentally measured thrust force, torque, and workpiece temperature. An inverse method was applied and the most suitable Coulomb coefficient of friction was determined to be 0.7. Three FEM techniques were utilized to achieve the convergence and efficient FEM solution in friction drilling.

The FEM analysis generated detailed data that were difficult to measure experimentally. The model showed that the peak temperature of the Al 6061-T6 workpiece was high, $\sim 580^\circ\text{C}$, close to the melting temperature. The deformed mesh and distributions of stress and temperature from FEM analysis effectively demonstrated how the work-material heated up, softened, and formed the bushing. The work material flowed in the rotational direction around the tool confirming that 3D FEM analysis was required.

The model developed in this study can be further improved by including the tool temperature and deformation analysis, the use of a more comprehensive friction model, and the development of a tool penetration model without using the element deletion. The experimental measurements of thrust force, torque, and temperature [6] suggest that the coefficient of friction varies throughout the friction-drilling process. But, research is still lacking about how it changes and depends on sliding speed, contact pressure, temperature, etc., and is a topic for future work. A more complete FEM will enable a more accurate simulation and lead to better prediction of residual stresses and material deformation in the final part for different tool geometries in friction drilling.

Acknowledgment

This research is sponsored by Oak Ridge National Lab, managed by UT-Battelle LLC. Program management and technical

guidance by Dr. Phil Sklad, Dr. Zhili Feng, and Dr. Peter Blau are greatly appreciated.

References

- [1] van Geffen, J. A., 1976, "Piercing Tools," US Patent No. 3,939,683.
- [2] van Geffen, J. A., 1979, "Method and Apparatuses for Forming by Frictional Heat and Pressure Holes Surrounded Each by a Boss in a Metal Plate or the Wall of a Metal Tube," US Patent No. 4,175,413.
- [3] van Geffen, J. A., 1979, "Rotatable Piercing Tools for Forming Holes Surrounded Each by a Boss in Metal Plates or the Wall of Metal Tubes," US Patent Number, 4,177,659.
- [4] van Geffen, J. A., 1980, "Rotatable Piercing Tools for Forming Bossed Holes," US Patent No. 4,185,486.
- [5] Miller, S. F., Blau, P., and Shih, A. J., 2005, "Microstructural Alterations Associated With Friction Drilling of Steel, Aluminum, and Titanium," *J. Mater. Eng. Perform.*, **14**(5), pp. 647–653.
- [6] Miller, S. F., Wang, H., Li, R., and Shih, A. J., 2006, "Experimental and Numerical Analysis of the Friction Drilling Process," *ASME J. Manuf. Sci. Eng.* **128**(3), pp. 802–810.
- [7] Miller, S. F., Blau, P., and Shih, A. J., 2006, "Tool Wear in Friction Drilling," *Int. J. Mach. Tools Manuf.* (to appear).
- [8] Miller, S. F., Tao, J., and Shih, A. J., 2005, "Friction Drilling of Cast Metals," *Int. J. Mach. Tools Manuf.*, **46**(12–13), pp. 1526–1535.
- [9] Feng, Z., Santella, M. L., David, S. A., Steel, R. J., Packer, S. M., Pan, T., Kuo, M., and Bhatnagar, R. S., 2005, "Friction Stir Spot Welding of Advanced High-Strength Steels—A Feasibility Study," SAE Tech. Paper No. 2005-01-1248.
- [10] Chao, Y. J., Qi, X., and Tang, W., 2003, "Heat Transfer in Friction Stir Welding—Experimental and Numerical Studies," *ASME J. Manuf. Sci. Eng.*, **125**(1), pp. 138–145.
- [11] Schmidt, H., and Hattel, J., 2005, "A Local Model for the Thermomechanical Conditions in Friction Stir Welding," *Modell. Simul. Mater. Sci. Eng.*, **13**, pp. 77–93.
- [12] Soundararajan, V., Zekovic, S., and Kovacevic, R., 2005, "Thermo-Mechanical Model With Adaptive Boundary Conditions for Friction Stir Welding of Al 6061," *Int. J. Mach. Tools Manuf.*, **45**, pp. 1577–1587.
- [13] Awang, M., Mucino, V. H., Feng, Z., and David, S. A., 2005, "Thermo-Mechanical Modeling of Friction Stir Spot Welding (FSSW) Process: Use of an Explicit Adaptive Meshing Scheme," SAE 2005 World Congress, Apr. 13, Detroit.
- [14] Kakarla, S. S. T., Muci-Kuchler, K. H., Arbogast, W. J., and Allen, C. D., 2005, "Three-Dimensional Finite Element Model of the Friction Stir Spot Welding Process," *Friction Stir Welding and Processing III, 2005 TMS Annual Meeting*, San Francisco, Feb. 13–17, pp. 213–220.
- [15] Soo, S. L., Aspinwall, D. K., and Dewes, R. C., 2004, "3D FE Modeling of the Cutting of Inconel 718," *J. Mater. Process. Technol.*, **150**, pp. 116–123.
- [16] Feng, Z., Gould, J. E., and Lienert, T. J., 1998, "Heat Flow Model for Friction Stir Welding of Aluminum Alloys," *Proc. of TMS Fall Meeting—Symposium on Hot Deformation of Aluminum Alloys II*, Oct 11–15, Rosemont, IL, Minerals and Materials Society, Warrendale, PA, pp. 149–158.
- [17] Buffa, G., Hua, J., Shivpuri, R., and Fratini, L., 2006, "A Continuum Based FEM Model for Friction Stir Welding—Model Development," *Mater. Sci. Eng., A*, **419**, pp. 389–396.
- [18] Serway, S., 2000, *Physics for Scientists and Engineers*, 5th ed, Saunders College, PA.
- [19] ABAQUS, 2004, ABAQUS/EXPLICIT User's Manual, vol. 6.5, Providence, RI.
- [20] Servis, D., and Samuelides, M., 2006, "Implementation of the T-Failure Criterion in Finite Element Methodologies," *Comput. Struct.*, **84**, pp. 196–214.
- [21] Chao, Y. J., and Qi, X., 1998, "Thermal and Thermo-Mechanical Modeling of Friction Stir Welding of Aluminum Alloy 6061-T6," *J. Mater. Process. Manuf. Sci.*, **7**, pp. 215–233.
- [22] Nicholas, T., 1981, "Tensile Testing of Materials at High Rates of Strain," *Exp. Mech.*, **21**, pp. 177–185.
- [23] Altenhof, W., and Ames, W., 2002, "Strain Rate Effects for Aluminum and Magnesium Alloys in Finite Element Simulations of Steering Wheel Armature Impact Tests," *Fatigue Fract. Eng. Mater. Struct.*, **25**, pp. 1149–1156.